FISEVIER

Contents lists available at ScienceDirect

ISPRS Journal of Photogrammetry and Remote Sensing

journal homepage: www.elsevier.com/locate/isprsjprs





Amazon forest spectral seasonality is consistent across sensor resolutions and driven by leaf demography

Nathan B. Gonçalves ^{a,b,c,*}, Ricardo Dalagnol ^{d,e,f}, Jin Wu ^{g,h}, Aline Pontes-Lopes ^d, Scott C. Stark ^{a,b}, Bruce W. Nelson ^c

- ^a Michigan State University, Department of Forestry, College of Agriculture & Natural Resources, East Lansing, MI, USA
- ^b Program in Ecology, Evolution, and Behavior, Michigan State University, East Lansing, MI, USA
- ^c Brazilian National Institute for Amazon Research INPA, Brazil
- d Earth Observation and Geoinformatics Division, National Institute for Space Research-INPE, São José dos Campos, SP, Brazil
- e Center for Tropical Research, Institute of the Environment and Sustainability, University of California, Los Angeles, Los Angeles, CA 90095, USA
- f NASA-Jet Propulsion Laboratory, California Institute of Technology, Pasadena, CA 91109, USA
- g School of Biological Sciences, The University of Hong Kong, Pokfulam Road, Hong Kong, China
- h State Key Laboratory of Agrobiotechnology, The Chinese University of Hong Kong, Shatin, Hong Kong, China

ARTICLE INFO

Keywords: Tropical forest Dry season green-up Enhanced Vegetation Index Green chromatic coordinate Phenocam Leaf demography Central Amazon Drought

ABSTRACT

Controversy surrounds the reported dry season greening of the Central Amazon forests based on the Enhanced Vegetation Index (EVI) from the Moderate Resolution Imaging Spectroradiometer (MODIS). As the solar zenith angle decreases during the dry season, it affects the sub-pixel shade content and artificially increases Nearinfrared (NIR) reflectance and EVI. MODIS' coarse resolution also creates a challenge for cloud and terrain filtering. To reduce these artifacts and then validate MODIS seasonal spectral patterns we use 16 years of 1 km resolution MODIS-MAIAC (Multi-Angle Implementation of Atmospheric Correction) images, corrected to a nadir view and 45° solar zenith angle, together with an improved cloud filter. Then we show that the 30 m Landsat-8 Operational Land Imager (OLI) surface reflectance over two Landsat scenes provides independent evidence supporting the MODIS-MAIAC seasonality for EVI, NIR, and GCC (an additional important vegetation index, green chromatic coordinate). Our empirical method for controlling for sun-sensor geometry effects in Landsat scenes encompasses the use of seasonally distinct images that have similar solar zenith angles and cloud-free pixels on flat uplands having the same phase angle. We extended this validation to nine Amazon sub-basins comprising ~546 Landsat-8 images. Our study shows that the dry-season green-up pattern observed by MODIS is corroborated by Landsat-8, and is independent of satellite data artifacts. To investigate the mechanisms driving these seasonal changes we further used Central Amazon tower-mounted RGB cameras providing a 4-year record at the Amazon Tall Tower (ATTO, 2°8'36"S, 59°0'2"W) and a 7-year record at the Manaus k34 tower $(2^{\circ}36'33''\ S,\ 60^{\circ}12'33''W)$ to obtain monthly upper canopy green leaf cover (a proxy for Leaf Area Index - LAI) and monthly leaf age class abundances (based on the age since leaf flushing, by crown). These were compared to seasonal patterns of GCC and EVI in small MODIS-MAIAC windows centered on each tower. MODIS-MAIAC GCC was positively correlated with newly flushed leaves ($R^2 = 0.76$ and 0.44 at ATTO and k34, respectively). EVI correlated strongly with the abundance of mature leaves ($R^2 = 0.82$ and 0.80) but was poorly correlated with LAI $(R^2 = 0.20 \text{ and } 0.41, \text{ respectively})$. Therefore, seasonal spectral patterns in the Central Amazon are likely controlled by leaf age variation, not quantity of leaf area.

1. Introduction

Sun-sensor geometry influences vegetation canopy reflectance and

can cause seasonal artifacts, a problem that underlies a long-lasting debate about the detection and magnitude of leaf phenological phenomena in Amazon evergreen forests (Saleska et al., 2007; Galvão et al.,

E-mail addresses: nathanborges@gmail.com (N.B. Gonçalves), dalagnol@ucla.edu (R. Dalagnol), jinwu@hku.hk (J. Wu), alineplopes@gmail.com (A. Pontes-Lopes), scstark@msu.edu (S.C. Stark), bnelsonbr@gmail.com (B.W. Nelson).

https://doi.org/10.1016/j.isprsjprs.2022.12.001

Received 21 December 2021; Received in revised form 30 September 2022; Accepted 1 December 2022 Available online 4 January 2023

^{*} Corresponding author.

2011; Morton et al., 2014; Bi et al., 2015; Saleska et al., 2016; Hashimoto et al., 2021). The resolution of this controversy is crucial for future efforts to understand how climate anomalies may affect leaf phenology and primary productivity in the Amazon. The main issue arises from the fact that when the Moderate Resolution Imaging Spectroradiometer (MODIS) Terra (and Landsat-8 OLI) platforms pass over the Central Amazon during the drier months from July to November, solar zenith angles decrease by approximately 15°. This causes a progressive decrease in sub-pixel shade content and consequent increase in the Nearinfrared (NIR) reflectance and Enhanced Vegetation Index (EVI), which may cause apparent greening as an artifact. According to Morton et al. (2014), sun-sensor effects may fully explain the dry season green-up observed in MODIS EVI.

The MAIAC (multi-angle atmospheric correction) adjustment to MODIS (Lyapustin et al., 2012; Dalagnol et al. 2022) removes artifacts of view and illumination geometry and has improved cloud detection and filtering. Band reflectances are corrected to a nadir view and a fixed solar zenith angle by applying a Bidirectional Reflectance Distribution Function (BRDF) inversion model that requires a minimum set of three observations of each pixel within each 8-day temporal mosaic. Apparently free of sun-sensor artifacts, MODIS-MAIAC confirms that about half the amplitude of the uncorrected MODIS dry-season green-up pattern for EVI in the Central Amazon is real (Bi et al., 2015, Guan et al., 2015, Saleska et al., 2016). However, MODIS data is captured at 250 m resolution and MAIAC is generated with a spatial resolution of 1 km, leaving doubts as to the full removal of clouds and of the influence of topographic shade in the BRDF inversion (Galvão et al., 2016). Cloud cover can also influence the BRDF inversion, as only a few pixels are available during the wettest periods.

Therefore, it is important to confirm the coarse resolution of MODIS-MAIAC-derived seasonal spectral patterns with independent sensors with a finer spatial resolution, as haze, clouds, cloud shadows, and terrain artifacts are more easily detected. To this end, we gathered data from Landsat-8 OLI imager – we used specifically Landsat-8 OLI due to its superior radiometric resolution when compared to past Landsat missions – and two tower-mounted RGB cameras. The 30 m Landsat-8 Operational Land Imager (OLI) provides a bridge between the small area (<10 ha) of tower-based detections of seasonal changes in crown color, leaf age mix and leaf amount at one spatial resolution extreme and coarse spatial-resolution MODIS at the other extreme.

Robust BRDF corrections of Landsat-8 OLI for seasonal comparisons are, nevertheless, still not feasible because of the 16 day revisit time and the extremely cloudy Amazon wet season. In spite of efforts to correct Landsat based on MODIS BRDF parameters (Roy et al., 2016), it would not be meaningful to compare MODIS MAIAC and corrected Landsat because they both use the similar Ross-Thick Li-Sparse model derived from MODIS (though MAIAC retrieves BRDF parameters differently; Lyapustin et al., 2012). A simpler and more reliable solution, to compare both products, takes advantage of the fact that the Landsat view angle is approximately fixed for each pixel and that the same solar zenith angle repeats four times per year at the hour of Landsat overflight near the equator. Landsat images having identical or very similar sun-sensor geometry are therefore available from different seasons of the year (Gonçalves et al., 2019). No BRDF correction is required for their comparison, so these Landsat images can be used to effectively validate the seasonal spectral patterns of MODIS-MAIAC.

To explain seasonal spectral patterns seen by MODIS-MAIAC, in terms of changing canopy leaf phenology, tower-mounted RGB cameras provide useful local-scale high-frequency data. While these operate only in the visible portion of the spectrum, RGB cameras provide data on upper canopy leaf age and leaf amount, which are jointly responsible for a large part of seasonal change in optical region canopy spectra. Tower-mounted RGB cameras have already contributed to elucidating the phenological drivers of seasonality in photosynthesis and photosynthetic efficiency at tower sites (Wu et al., 2016). The Leaf area index (LAI) seasonal variation in Central Amazon is small, ranging from 5.5 to

 $6.2\,\mathrm{m^2/m^2}$ levels (Brando et al., 2010), at which the spectral response to change in LAI nearly saturates (Ponzoni, Shimabukuro & Kuplich, 2007). On the other hand, leaf demography varies greatly across seasons, as also shown by tower-mounted cameras (Lopes et al., 2016). Together this suggests that seasonal differences in EVI are induced mainly by leaf age and less by seasonal changes in leaf amount. Supporting this expectation, Wu et al. (2018) drove a radiative transfer model with changes in leaf amount and leaf age from camera data, combined with bare branch spectral and leaf spectra for different leaf age classes . The radiative transfer model showed consistent seasonal patterns between predicted EVI and MODIS-MAIAC EVI seasonal patterns, with primary attribution to changing leaf age.

Nonetheless, an empirical comparison of canopy spectral attributes at the scales of tower cameras (~ 1 m), Landsat-8 (30 m) and MODIS-MAIAC (1 km) has yet to be undertaken and will contribute to our understanding of the reliability of the seasonal spectral patterns detected by MODIS (Maeda et al., 2016) and the leaf- and canopy- scale drivers of these seasonal patterns in tropical forests. Our objectives address two major questions that, if properly answered, offer a much more complete understanding of the Amazon seasonal green-up by examining different spectral remote sensing instruments and platforms from coarse to very high resolutions:

First, we ask if the Landsat-8 OLI (finer resolution) confirms the seasonal patterns observed in the main spectral indices and bands of interest from the MODIS-MAIAC (coarser resolution) related to the dry season green-up debate. We examine the Green chromatic coordinate (GCC), NIR reflectance and EVI. Here, we use several Landsat-8 OLI image dates with pixel subsets selected to show clear seasonal contrast in these MODIS-MAIAC indicators, but also having minimal differences in their view and illumination geometries while controlling for a series of artifacts. Second, having reinforced our confidence in the MODIS-MAIAC spectral signal, we ask which biophysical attributes of the canopy – leaf amount or leaf age – derived from two Phenocam systems in the central Amazon best explain the seasonal spectral patterns of GCC and EVI.

2. Material and methods

2.1. Landsat-8 OLI processing

Our first question is addressed by employing three different approaches to account for sun-sensor geometry in Landsat-8 data so that we could compare spectral information between images acquired during different seasons.

2.1.1. Approach 1 - controlling for phase angle, while allowing minor differences ($<\sim$ 4°) in solar zenith angle

In this approach, we looked for surface reflectance Landsat-8 OLI images in the central Amazon acquired from the same Worldwide Reference System (WRS) scene at various times of the year and with similar solar zenith angles. Seasonal BRDF artifacts are mostly caused by the solar zenith angle (Galvão et al., 2011; Morton et al., 2014). Up to four times during the year, the solar zenith is identical within a few degrees of the equator and during the 10:00 h local Landsat passing. As view angles vary across the image, BRDF artifacts are also likely to be present. In order to represent the effects of sun-sensor geometry, the phase angle of each pixel could be calculated (Maeda and Galvão, 2015). This is the angle between a pixel's sensor view vector and its solar illumination vector (Bi et al., 2015). Phase angle of each pixel combines the main components of sun-sensor geometry effects on a pixel's reflectance into one variable (Maeda and Galvão, 2015). The calculation is (Eq. (1)):

$$\begin{aligned} Phase_angle & = ACOS[(COS(SVZ) \times COS(SZA)) + (SIN(SVZ) \\ & \times SIN(SZA) \times COS(RAA)] \end{aligned} \tag{1}$$

where SVZ is the sensor view zenith angle, SZA is the sun zenith angle and RAA is the relative azimuth angle. SIN and COS are sine and cosine respectively.

When the difference in SZA between image acquisitions – from different seasons that are to be compared – is small at the scene center, it is possible to find pixels with the same phase angle in distinct parts of the different images. Pixels with the same phase angle can have different solar azimuth angles, thus different amounts of topographic shade, but there should be no bias in this noise if topographic features have no preferred azimuthal orientations. In the Central Amazon, image dates with small ($<\sim4^\circ$) difference in solar zenith and having pixels with shared phase angles were chosen to coincide with strong seasonal differences in the EVI and GCC vegetation indices from local MODISMAIAC on those same dates, and to also coincide with seasonally distinct phenological periods detected in tower RGB camera data (Lopes et al., 2016).

Given the restrictions we mentioned above and the intense cloud cover towards the wet season we were only able to obtain three usable images with similar solar zenith angles and in three distinct phenological periods for the Landsat scene 230 63 (Fig. 1B, Fig.S9), centered at 4°12'S, 59°12'W which is 160 km south-southeast of Manaus city, Brazil. One image was from the mid wet season (Feb 11, 2016 - DOY 42) when tower-mounted cameras at Manaus-k34 and Amazon Tall Tower Observatory (ATTO) sites show very little leaf flushing or pre-flush leaf abscission (few bare crowns). Dark green leafy crowns predominate across the phenocam views. A second image was from the wet to dry season transition (May 25, 2013 - DOY 145), when old leaves are abundant and LAI is near its annual mean (Wu et al., 2016). The third image was from the dry season (August 03, 2015 - DOY 215), when leafless crowns are most abundant and recently flushed crowns (0, 1 or 2 months since flush) are even more abundant. The image region selected for this approach has an average dry season length of 2.9 months based on (from TRMM 3b43 v7) product. This is close to the dry season length at both the ATTO and Manaus k34 tower sites (Fig. 1B), where phenocams we analyzed here were installed. Solar zenith angles at the scene center for the selected Wet (DOY 42), Wet-to-Dry (DOY 145) and Dry (DOY 215) season images were 32.15°, 36.18° and 36.13°. Only

pixels with the same phase angles were compared. EVI was calculated as in (Huete et al., 2006; Solano et al., 2010; Galvão et al., 2011) and GCC was calculated as in phenological monitoring RGB cameras but using reflectance instead of digital number (Sonnentag et al., 2012; Lopes et al., 2016) (Eq. S1 and Eq. S2, Supplementary data).

2.1.2. Approach 2 - fixed nadir view and fixed solar zenith angle for NIR and EVI

In some cases, two sets of pixels may have the same phase angle, but different relative azimuth angles, such that one date's pixels are observed under forward scattering geometry (Bi et al., 2015), while the other date's under backscatter, which can affect spectral data (Moura et al., 2012). We therefore use a more conservative method. We now compare two images with nearly identical solar zenith (based on metadata for the scene center) and restricted the sensor view angle to $<0.5^{\circ}$ off-nadir, i.e., to a narrow strip of pixels close to the orbital track (Gray rectangle in Fig. 1B and in Fig.S9). Pitfalls of sun-sensor geometry are theoretically fully resolved.

Finding cloud-free Landsat-8 image areas that meet these more conservative conditions is even more challenging than approach 1. We found a pair of images of the scene 230 61 for 2015 (Fig. 1B), centered at 1° 27'S, 58° 44'W (225 km NE of Manaus, and 90 km NNE of the ATTO tower phenocam), having SZA difference of only 0.6°. The average dry season length is 3.4 months (from TRMM 3b43 v7). One image was from the late Wet season (15 May 2015, DOY 135) with 33.00° SZA. The other was from the early Wet season (09 December 2015, DOY 343) with a scene center SZA of 32.44°. These two Landsat dates are useful for confirming a very large expected difference in EVI and NIR (as seen in local MODIS-MAIAC), but no strong seasonal difference in GCC is expected, as seen in the nearby tower phenocam data. We therefore extracted only EVI and NIR reflectance from Landsat and from MODIS-MAIAC for these two dates. NIR is a proxy for EVI and is less affected by haze than other bands that comprise EVI (Morton et al., 2014; Bi et al., 2015).

All five Landsat-8 images analyzed for both approaches 1 and 2, were surface reflectance collection 1 level 2 products downloaded from the USGS Earth Explorer platform. For all five dates we used only upland

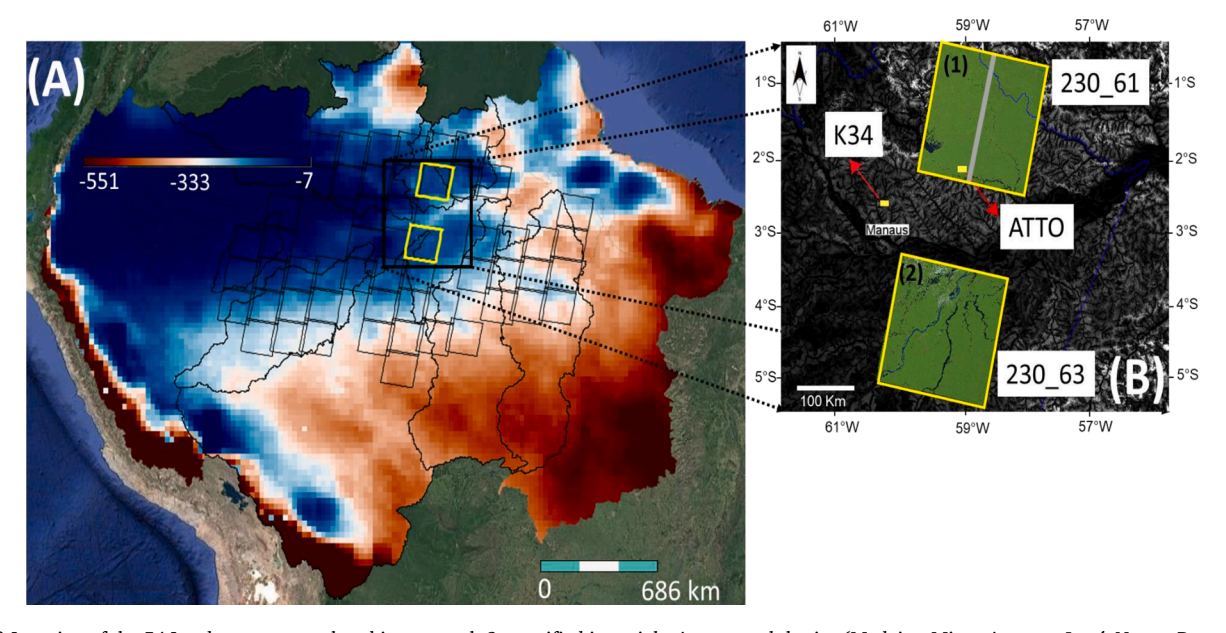


Fig. 1. A) Location of the 54 Landsat scenes analysed in approach 3, stratified into eight Amazon sub-basins (Madeira, Minor Amazon Jutaí, Negro, Purus, Tapajós, Trombetas, Xingu, and Minor Amazon Uatumã); The base image shows the long-term mean of the local MCWD (Maximum climate water deficit), a combined measure of dry season length and intensity (Malhi et al., 2009). B) The two Landsat scenes used in approaches 1 and 2; B1) 230_61 and B2) 230_63 scene, the two tower-mounted RGB cameras: k34 and ATTO, and the small windows considered in MAIAC analysis (to Q2); The bottom image in is a grayscale HAND (height above the nearest drainage). The RGB images are Landsat Look Natural Color Images. B1 also depicts the near nadir region of interest (ROI) in gray used to analyze data on scene 230_61 with approach 2.

areas, i.e., excluding rivers, streams, and floodplains. To this end, we filtered all 30 m Landsat pixels having less than 15 m Vertical Distance to Channel Network (Conrad et al., 2015), an algorithm which uses 30 m Shuttle Radar Topography Mission (SRTM) elevation data as the input. To minimize the effects of topographic shade, we accepted only those Landsat pixels with slope < 4°. We masked all clouds and cloud shadows in Landsat using an adaptation of the Multi-temporal Cloud Masking (MCM) method of Candra et al. (2016). This algorithm uses the difference of the reflectance between a target image, free from clouds and cloud shadows, and a cloud-contaminated image in order to distinguish between clear pixels and cloud-contaminated pixels. To detect clouds, we used the difference thresholds for band 3 (Green) and for band 4 (Red). For cloud shadows we used the difference threshold of band 6 (Swir 1). For each difference image, we selected an empirical threshold that maximized cloud and cloud shadow detection. We followed up with a careful visual inspection of unmasked areas to detect errors of omission. We further accepted only pixels with NDVI > 0.75. The 0.75 NDVI threshold ensures that no cloud or cleared forest area will be included in the analysis if prior masking or visual inspection fails. For comparisons and models, only non-masked pixels from both seasonally distinct images were used. We assume that the sets of usable pixels available on each date represent the average scene signal on that date. Since we are always comparing flat, well-drained old-growth upland forests within the same 185 km \times 185 km scene, this is a reasonable assumption. In all cases, the sampled pixels are from the same forest type and have very similar climatic and edaphic characteristics. Furthermore, at this spatial scale, BRDF-corrected MODIS EVI spatial variations are very low (Dalagnol et al., 2022). This assumption is also necessary because over the acceptable dates, only a small number of pixel positions are cloudfree. Aside from that, the phase angle of a pixel rarely stays the same throughout the year given the significant variation in solar azimuth, particularly in approach 1, where we do not have an almost Nadir view. It is therefore challenging, if not impossible, to compare the same pixel over time with the same phase angle.

Given the above-mentioned limitation of not spatially matched pixels being compared through time, we also investigated whether any spatial structure was influencing our results by running general additive models including pixels' coordinates as a smooth term while accounting for other undesirable variables (*Eq. S3, Supplementary data*). We have now analyzed only the pixels that are available, following the masking procedure explained before, intersecting the three images in approach 1 and the two images in approach 2.

All analyses were performed using the statistical and computational platform R. the raster package (Hijmans, 2016; R Development Core Team, 2017). GAM models were run using mgcv and visualized using mgcViz (Wood, 2017; Fasiolo et al., 2019)

2.1.3. Approach 3 - fixed nadir view at the sub-basin scale:

In approaches 1 and 2, just two Landsat scenes and five dates, respectively, were examined. Four of the dates fell during the 2015–2016 El Nino drought years. There is evidence that inter- and intra-annual greenness are impacted by Amazonian droughts (Saleska et al., 2007; Yang et al., 2018; Gonçalves et al., 2020). To amplify our findings to the continental scale of the Central Amazon wet forests, two Landsat scenes are likely insufficient. We used Google Earth Engine (GEE) to broaden our investigation to more Landsat scenes and also circumvent several limitations of approaches 1 and 2 (Fig. 1A). We utilized the USGS Landsat-8 Surface Reflectance (Collection and Tier 1) product at the native 30 m resolution for the period 2013 to 2021, omitting the extreme drought of 2015–2016. The current focus is on confirming the MODIS-MAIAC seasonal patterns of EVI alone.

Based on image metadata supplied by GEE for the scene centers, we searched all Landsat-8 images with solar zenith angles between 29° and 38° and cloud cover < 45% in the Central Amazon (Fig. 1A). For each scene, 60,000 pixel positions were randomly selected based on a single image date within an area of $+/- 0.5^{\circ}$ off the nadir view angle (see

Fig. 1B and Fig. S10 for an illustration). In the following step, we extracted Landsat-8 spectral data from the same 60,000 pixels postions from each image within each scene of a total of 546 images. The nearnadir ROIs were defined using the same single image date from each path-row scene. We here assume that the nadir ground track line and the view angle for any pixel on the ground to be constant over time. Additionally, we assume that the solar zenith angle remains constant during the brief time ($\sim 30 \, \mathrm{s}$) it takes to acquire each image. As with approach 2, by limiting the analysis to a near-nadir view, this approach maintains a nearly fixed phase angle for any solar zenith angle regardless of the solar azimuth and theoretically resolves the forward-scatter / backscatter issue. Due to the fact that only the solar zenith angle will contribute significantly to reflectance anisotropy, we only need to control for this single covariate.

Similar to approach 1 and 2, we implemented the Candra et al. (2016) cloud masking procedure. Given the large data set, we could not inspect the mask manually. Therefore, we added a mask buffer of 500 m to all pixels classified as clouds or cloud shadows. We also employed Landsat-8 QABits to filter pixels with cloud, cloud shadow, or aerosol contamination. We further only considered pixels with NDVI > 0.75 and reduced terrain slope artifacts by considering only pixels with slope $<4^{\circ}$ and Height Above Nearest Drainage (HAND) > 10 m. We used the global 30X30m HAND product (Donchyts et al., 2016) available on the GEE platform. To mask flooding areas not completely removed by HAND (e. g., areas associated with interfluvial perched water tables, flat areas where the channel network required by HAND is nonexistent or poorly defined), we relied on Hess et al. (2015). Lastly, we used PRODES (Brazilian Amazon Deforestation Monitoring Program) data (Valeriano et al., 2004) to mask deforestation and/or secondary forest.

Due to the combined limitations imposed by near-nadir view, flat upland terrain, cloud-free pixels, and the GEE platform limit on exporting data, Landsat-8 image pairs having usable pixels with the same SZA were rarely available from the same scene in different seasons. Hence, we decided to cluster Landsat-8 scenes into Amazon sub-basins (Fig. 1A, Fig. S10, Venticinque et al., 2016).

We focused on eight Amazon sub-basins, shown in Fig. 1A, with 54 scenes and 546 usable Landsat-8 images acquisitions. In order to test if Landsat-8 EVI seasonality is consistent with MODIS-MAIAC EVI, we started by identifying contrasting MODIS-MAIAC EVI seasonal periods (See methods for MODIS-MAIAC) and categorizing them as either HIGH or LOW EVI time periods for each clustered sub-basin (Fig. S10). It is crucial to emphasize that this categorization was carried out because, despite the clustering of numerous Landsat-8 scenes by sub-basins, there were not enough pixels available for all months of the year, especially during the wettest months, preventing us from being able to accurately model Landsat-8 EVI continuous monthly averages while controlling for the sun zenith angle using conventional linear models.

We follow the analyses by running mixed effects models for each subbasin including all available pixels, after the masking procedure delineated before. We used the pixel identity as a random effect and controlled for several confounding factors. We used the local EVI time periods (HIGH/LOW) as a categorical variable, based on MODIS-MAIAC data (Eq. (2)) and statistically controlled the solar zenith angle and HAND elevation. Additionally, we allowed the categorical time periods for local EVI to interact with the solar zenith angle. The variable pixel fraction (Eq. (2)) takes into account the possibility of varying numbers of cloud-free pixels between HIGH and LOW time periods. Furthermore, we compared changes in MODIS-MAIAC seasonal amplitude with changes in Landsat-8 across all sub-basins. To calculate and display the partial effects of each category (HIGH/LOW) while other predictors are held constant, we used the R package effects (Fox, 2003).

$$\begin{split} \text{Landsat8_EVI} &= \alpha + \beta 1^*(\text{MODIS_HIGH/LOW}) + \beta 2^*(\text{Solar Zenith}) \\ &+ \beta 3^*(\text{HAND}) + \beta 4^*(\text{Fraction}) + \beta 5^*(\text{Scene}) \\ &+ \beta 6^*(\text{MODIS_HIGH/LOW})^*(\text{Solar Zenith}) + (1|\text{ID}) \\ &+ \ \varepsilon \end{split}$$

where Landsat8_EVI (continuous) is the dependent variable; MOD-IS_HIGH/LOW (categorical variable) are the two contrasting local EVI time periods for each sub_basin analyzed as seen by MODIS-MAIAC (See Fig. S10 for further explanation); Solar zenith (continuous) is the solar zenith angle at the center of each analyzed image; HAND (continuous) is the height above the nearest drainage; Fraction (continuous) is the fraction of usable pixels within a Landsat image near-nadir ROI; Scene (categorical) is the WRS scene that a certain pixel belongs to; and ID (categorical) is the unique pixel identity throughout the time series.

To determine whether any spatial structure was affecting our modeling and to be able to generate temporal continuous seasonal curves, we also ran generalized additive models (GAM), but only for the Madeira sub-basin, in which we were able to obtain more usable data and therefore could make more consistent predictions. We used GAMs because they are more flexible to non-linear data and less memory intensive when including the spatial structure. The spatial structure in the model is now incorporated via a smooth term using the pixels' coordinates, along with the day of the year (DOY) and sun zenith angle, following Eq (3). Only the seasonality of the first 250 days of the year is modeled given the lack of data in months with sun zeniths $< 29^{\circ}$. We set the number of basis functions (k) to 5 for the variable DOY, given the lack of data in several parts of the period to limit the smoothness and overfit. We additionally modeled GCC seasonality within the same period and same area using a similar method.

$$\begin{aligned} \text{Landsat8_VI} &= \alpha + \text{s(DOY)} + \text{s(Lat,Long)} + \text{s(Solar Zenith)} + (\text{HAND)} \\ &+ (\text{Fraction}) + (\text{Scene}) \ + \ \varepsilon \end{aligned} \tag{3}$$

where <code>Landsat8_VI</code> (continuous) is the dependent vegetation index variable (EVI or GCC); <code>DOY</code> is the continuous day of the year; Solar zenith (continuous) is the solar zenith angle at the center of each analyzed image; <code>HAND</code> (continuous) is the height above the nearest drainage; Fraction (continuous) is the fraction of usable pixels within a Landsat image near-nadir ROI. S term denotes the smooth term. K is the number of basis functions that was set to 3 for solar zenith since an almost linear relationship is expected and set to 5 to DOY to allow more wiggling, however limiting the same due to lack of data in some periods.

2.2. MODIS-MAIAC processing

The MAIAC product was generated with empirical BRDF corrections to an apparent view zenith angle of 0° (nadir view) and an apparent solar zenith of 45°. Temporal resolution was 16 days and spatial resolution of 1 km. MAIAC BRDF correction relies on several cloud-free measurements of a pixel for each of the eight days, during which the sun-sensor geometry must vary widely (Lyapustin et al., 2012; Moura et al., 2015; Dalagnol et al. 2022). The dataset used here is part of the early versions of the AnisoVeg product (https://zenodo. org/record/6561351#. YyxaEHbMJPY, Dalagnol et al. 2022). In order to compare MODIS-MAIAC and Landsat-8 to answer our first question, we obtained MODIS observations that geographically match the usable areas of two or more seasonally distinct Landsat-8 images within a scene as mentioned in the previous section. We used the official Brazilian deforestation data known as PRODES (Valeriano et al., 2004) to mask deforestation and secondary forest in both MODIS and Landsat We used 1 km resolution HAND data (Height Above Nearest Drainage) available at www.dpi.inpe.br/Ambdata to mask rivers, streams and seasonally flooded areas (Rennó et al., 2008) in the MODIS images. We did not apply a slope restriction to the MODIS data.

(2)

We calculated the spatial average of each spectral index or band over the usable Landsat scene area for each 16-day MODIS-MAIAC period in the time series from January 2001 to September 2016. We chose the five MODIS-MAIAC 16d periods that included the five dates on which usable Landsat images were collected for approaches 1 and 2. In approach 2 of the scene 230_61 only MAIAC data within the near nadir ROI was analyzed. EVI and GCC calculations for MODIS-MAIAC were the same as for Landsat-8 data.

In approach 3, in order to obtain MODIS-MAIAC EVI seasonality we used the same near-nadir ROI (Region of Interest) established in each of the analyzed Landsat-8 scenes to gather the EVI data within each subbasin (see Fig. 1B and Fig. S10 for an illustration). At each sub-basin, we modeled MAIAC-EVI seasonality using a mixed modeling approach, excluding times of droughts and controlling for undesirable variables (Eq. (4)). Based on the MAIAC EVI seasonality, we identified contrasting HIGH/LOW seasonal EVI periods for each sub-basin. Contrasting HIGH/LOW seasonal EVI periods were selected based on the trade-off of more overlapping pixels and more variation in solar zenith angle in the Landsat-8 dataset (Fig. S10).

MODIS_EVI =
$$\alpha + \beta 1*(month) + \beta 2*(HAND) + \beta 3*(Scene) + (1|ID)$$
 + ε (4)

Where *MODIS_EVI* is the dependent variable (continuous) month is the month of the year; HAND is the height above the nearest drainage at 1 km resolution; ID is the MODIS pixel identity throughout the time series.

Additionally, we run generalized additive models (GAM) only for the Madeira sub-basin to check whether spatial structure impacted our modeling and to generate continuous seasonal curves for the same time period as the Landsat-8 data (between 2013 and 2021). We only included the first 250 days of the year, following the same method as described in Eq. (3).

To answer our second question, regarding possible biophysical drivers or triggers of MODIS spectral data, we used the spatial average from two windows of 8x11 MODIS-MAIAC pixels, each centered on a tower-mounted phenocam described in the next section. The window size was empirically chosen. Larger windows are likely to decrease noise, but may also include undesired cover types (e.g., open water, riparian forests, deforestation, and secondary forests). We used MODIS-MAIAC long run 16y seasonal averages as most years had limited data for the rainy season given the small window being considered. Using 16y averages also reduced the short-term noise which is common in MODIS data

2.3. Leaf demography processing

We monitored the upper canopy leaf phenology from July 2013 to mid-2016 at the ATTO tower site (2° 8'36"S and 59° 0'2"W) with an RGB Stardot Netcam model XL 3MP camera, set to an interpolated resolution of 2048 \times 1536 pixels. The camera was mounted 81 m above the ground and ~ 50 m above the forest canopy. Each of 270 upper canopy tree crowns was followed daily, always using images obtained under diffuse light (dense cloud shadow or overcast sky). At the k34 tower site (2°36'33" S, 60°12'33" W), we monitored from September 2010 to September 2016, with the same camera model, but mounted 51 above the ground. The image area at k34 included 42 upper canopy crowns. Using the date of each crown's abrupt leaf flush (which usually occurs once per year) as a marker, the age of each leaf cohort was determined (Lopes et al., 2016). We divided crowns that flushed monthly into three leaf age classes as suggested by Wu et al. (2016). Different transition ages were tested to find the abundance class that best correlated with MODIS derived local EVI for the two tower sites. We calculated a camera-based Leaf Area Index (LAI) as a linear function (y = 8.24*x-1.99) of the fraction of crowns that were leafy, following Wu et al.

(2016).

We compared the two correlations (EVI \times leaf age class abundance and EVI \times leaf amount) to determine which was the better predictor (and possible driver) of EVI seasonality. Additionally, we used the ProSAIL radiative transfer model (a combination of the PROSPECT leaf optical properties model and SAIL canopy bidirectional reflectance model) via the Hsdar package to examine the sensitivity of EVI to changes in LAI (Jacquemoud et al., 2009; Lehnert et al., 2019). Input leaf reflectance spectrum (and therefore the leaf age effect on EVI) was fixed in this model. Under these conditions, if LAI is a weak driver of a vegetation index with strong seasonality, then the seasonality is likely to be driven mainly by spectral changes in leafy canopies that are related to leaf age classes (Wu et al., 2018). We kept all other model parameters constant (Observer zenith angle $= 0^{\circ}$, Solar zenith angle $= 45^{\circ}$, Relative azimuth angle = 45°, Leaf angle distribution = Plagiophile) and let LAI vary. Note that the Relative azimuth angle parameter is not relevant when the observer's zenith angle is 0° (Nadir View). We simulated how EVI would vary with seasonal variations in LAI in four sites in the Amazon (Table S1). The Geoscience Laser Altimeter System (GLAS) LAI is from Tang and Dubayah (2017) for the central Amazon region in general; K67 LAI in the western Amazon is from Wu et al. (2016), k34 and ATTO LAI were estimated from the green crown fraction utilizing the equation of Wu et al. (2016).

3. Results

3.1. Testing if Landsat-8 OLI seasonal patterns of GCC, EVI and NIR are consistent with MODIS-MAIAC utilizing three different approaches

3.1.1. Approach 1 - controlling for phase angle, while allowing minor differences ($< \sim 4^{\circ}$) in solar zenith angle

Within the region of Landsat scene 230_63, 160 km SE of Manaus (Fig. 1B), we found strong seasonal change in GCC , peaking in the middry season (Fig. 2B, Fig. S1). For the three test dates, Landsat-8 corroborated MODIS-MAIAC GCC, showing the same temporal ordering of low-intermediate-high GCC for Wet (DOY 42) to Wet to Dry transition (DOY 145) to Dry (DOY 215) images (Fig. 2B, 2D). Amplitude changes were also similar, the low and high extremes of GCC were from the Wet (DOY 42) to Dry (DOY 215) dates of Landsat acquisitions (Fig. 2D). Over the same time period, the closest dates of MODIS-MAIAC GCC observations at the same area increased 3.8 \pm 0.07% (95%

Confidence interval). While we found a larger Landsat-8 GCC increase from the Wet (DOY 42) to Dry (DOY 215) images, $5.9\pm0.3\%$ (Fig. 2B). Landsat-8 data show that season has a clear effect on GCC when controlling for the phase angle (p $<0.001,\,F=1182)$ (Fig. 2B). However, the narrow range of Landsat phase angles shared between the three image dates (35-37°) had no influence on the temporal separation of GCC (p $=0.9,\,F=0.008).$ In other words, it is not necessary to control for the effect of phase angle on GCC when using seasonally distinct Landsat images with very similar solar zenith angles.

Within the region of the same 230_63 Landsat-8 scene 160 km SE of Manaus, EVI of MODIS-MAIAC showed a ranking of high-low-intermediate for Wet (DOY 42) to Wet to Dry transition (DOY 145) to Dry (DOY 215) (Fig. 2A). Over the whole scene the Wet (DOY 42) image was on average 3.14 \pm 0.02% higher than Wet to Dry transition (DOY 145) for the closest dates of MODIS-MAIAC EVI. The three Landsat-8 EVI images corroborated the MODIS-MAIAC seasonality and the observation for the closest dates, showing the same temporal ordering of high-low-intermediate EVI respectively for Wet (DOY 42) - Wet-Dry (DOY 145) - Dry (DOY 215) (Fig. 2A, Fig. 22C). The increase observed from Wet (DOY 42) to Wet-Dry (DOY 145) was higher for Landsat-8 EVI 6.9 \pm 0.4% compared to MODIS-MAIAC.

The same patterns and similar magnitudes for Landsat-8 EVI and GCC shown before are observed when using generalized additive models controlling for spatial structure and phase angle (Fig. S11)

3.1.2. Approach 2 - fixed nadir view and fixed solar zenith angle for NIR and EVI

For the Landsat-8 image pair from scene 230_61(Fig. 1B), 225 km NE of Manaus, for which solar zenith angles were nearly identical and spectral comparisons were restricted to $<0.5^{\circ}$ off-nadir view, we found an increase of 8.4 \pm 0.13% for EVI from May (DOY 135) to December (DOY 343) (Fig. 3B). Driving this EVI behavior was an increase of 13 \pm 0.16% in Landsat-8 NIR reflectance from May to December (Fig. 3A). This was again consistent with expectations from MODIS-MAIAC seasonality and with the values obtained with the closest temporal dates in 2015 where MODIS-MAIAC EVI increased 10.87 \pm 0.42% from May (DOY 144) to Dec (DOY 352) (Fig. S1, Fig. 3C).

While accounting for spatial structure and phase angle, Landsat-8 EVI and NIR results were also in line with previous findings (Fig. S12, just for NIR), displaying the similar pattern and magnitude of difference.

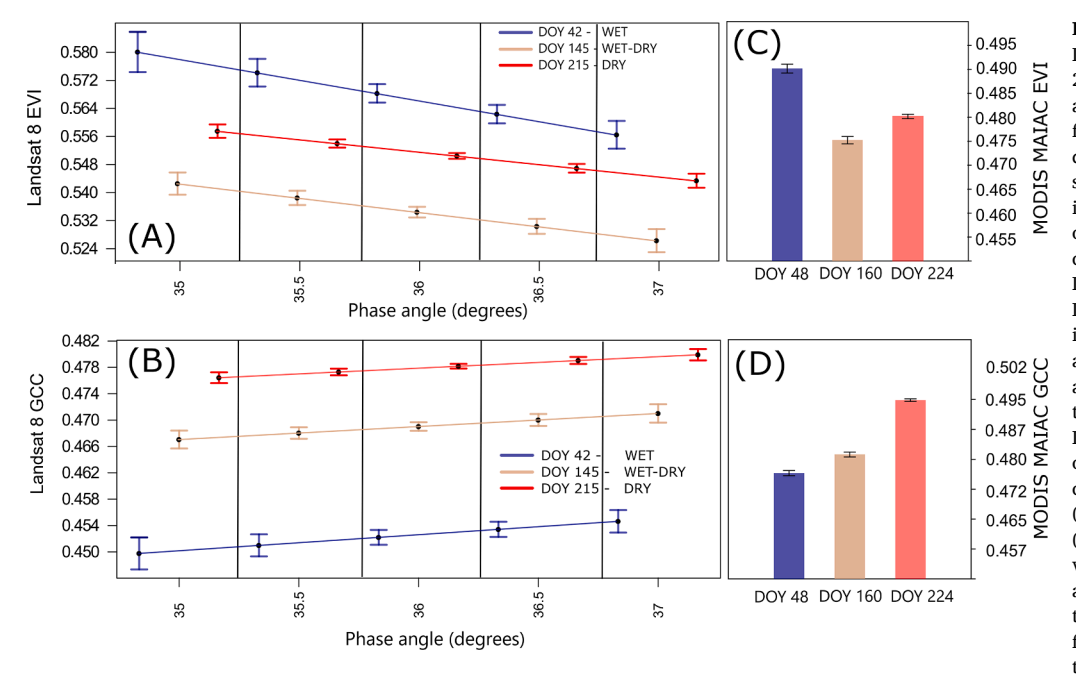


Fig. 2. EVI (A) and GCC (B) from Landsat-8 for upland forests in scene 230_63, controlling for phase angle (Xaxis). Error bars are 95% CI for each of five phase angle bins for each Landsat 8 date. Blue, brown and red colors represent Wet, Wet-to-Dry and Dry season image dates. (C) and (D) are the values of MODIS-MAIAC EVI and GCC for the closest day of the year relative to Landsat-8 acquisitions in which the Landsat-8 data acquisitions' date are included in the MODIS-MAIAC 16 day aggregation period. Vertical bars in (A) and (B) are meant to aid the visualization that regardless of phase angle Landsat-8 EVI and GCC show the same ordering of magnitude with the BRDF corrected MAIAC on the right (C) and (D). The lines linking the error bars in (A) and (B) are also intended to improve visualization showing the effect of phase angle on EVI and GCC. (For interpretation of the references to color in this figure legend, the reader is referred to the web version of this article.)

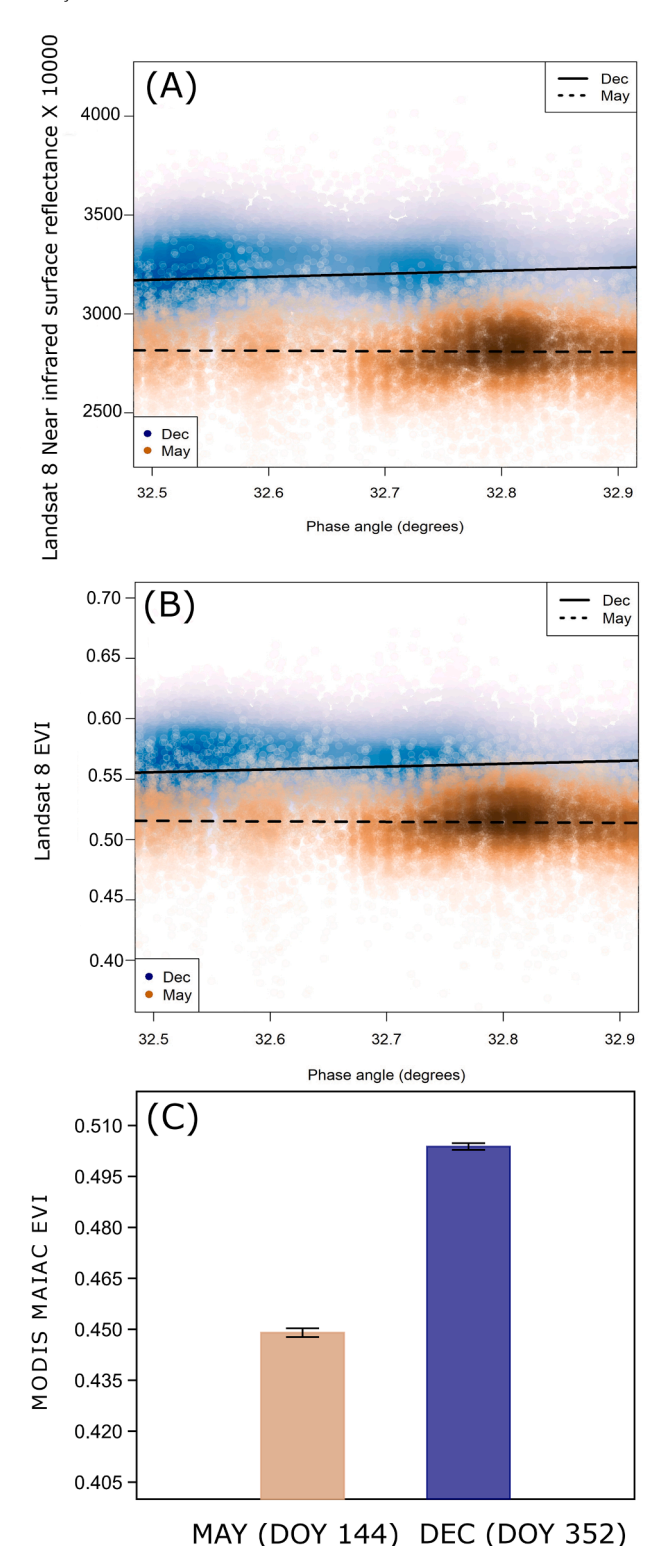


Fig. 3. Increase in near-nadir EVI (**A**) and NIR reflectance (**B**) in Landsat-8 scene 230_61 from May 2015 (DOY-135, brown) to December 2015 (DOY-343, blue), two images with nearly identical solar zenith angles and restricted sensor view angle ($<0.5^{\circ}$ off-nadir), to a narrow strip of pixels close to the orbital track. (**C**) MODIS-MAIAC EVI for the closest dates that include the two Landsat-8 acquisitions dates within the same near-nadir ROI. (For interpretation of the references to color in this figure legend, the reader is referred to the web version of this article.)

3.1.3. Approach 3 -Fixed nadir view at the sub-basin scale

Landsat-8 EVI controlled for sun-sensor geometry at sub-basin scale was consistent with BRDF corrected MODIS-MAIAC EVI seasonal spectral patterns throughout all sub-basins analyzed when comparing local periods categorized as HIGH and LOW EVI (Fig. 4; Fig. S5; Fig. S6; **Fig. S7**; **Fig. S8**; all p < 0.001) (The results remained the same when using only the NIR band and EVI without the blue band (Jiang et al., 2008), not shown). However, the percentage difference between periods was not always consistent. At some sub-basins the percentage difference between HIGH and LOW periods deviated from the 1:1 line (Fig. S3, red dots). Sub-basins in which the solar zenith angles of the available observations were broadly variable, on the other hand, the difference was numerically consistent between MODIS-MAIAC EVI and Landsat-8 EVI following the 1:1 line (Fig. S3, Black dots). EVI and GCC seasoality for both MAIAC and Landsat-8 were also consistent when controlling for the spatial structure while using generalized additive models (Fig. \$13) within the Madeira sub-basin. EVI and GCC seasonal curves for both sensors were highly correlated within the first 250 days of the year for the same period between 2013 and 2021.

3.2. Which biophysical attribute of canopy (leaf amount and leaf age) best explains the seasonal spectral patterns of GCC and EVI?

3.2.1. Biophysical control of MODIS-MAIAC GCC in the Central Amazon We use the abundance of crowns with 0–1-month age to represent the seasonal leaf flush at both sites with tower mounted RGB cameras (k34 and ATTO). Peaks in the abundance of recently flushed crowns are expected in the dry season. As shown by Fig. 5, seasonal MODIS-MAIAC GCC closely followed the abundance of leaves with 0–1 mo at ATTO site (${\rm R}^2=0.76,\,{\rm p}<0.001$) and at Manaus k34 (${\rm R}^2=0.43,\,{\rm p}<0.001$), after applying a one-month forward shift to the camera data. We also analyzed litter trap data for the k34 site in a normal rainfall year (Ourique et al. 2016). Litter production was collected between 2012 and 2013, about two kilometers from the k34 tower. The seasonal MODIS-MAIAC GCC (see. Fig. \$4) also showed strong association with litter production (${\rm R}^2=0.84,\,{\rm p}<0.001$).

3.2.2. Biophysical control of MODIS-MAIAC EVI in the Central Amazon

Seasonal MODIS-MAIAC EVI was strongly correlated with the abundance of the 'mature' leaf class in the upper canopy, of 2–7 months age (Fig. 6), at both ATTO (R 2 = 0.82, p < 0.001) and 2–8 months age at Manaus k34 (R 2 = 0.80, p < 0.001). Total LAI, on the other hand, was a poor predictor of EVI at ATTO (R 2 = 0.20, p = 0.018) and moderate predictor at Manaus – k34 (R 2 = 0.41, p = 0.002).

In our ProSail radiative transfer model, we used a fixed sun-sensor geometry consistent with MODIS-MAIAC (nadir view and 45° SZA), fixed leaf spectra and the LAI annual amplitude reported in Wu et al. (2016), of 5.5 to 6.2 $\rm m^2/m^2$, valid for the K67 site. The model results showed an LAI forcing effect of only 1.4% on predicted EVI. When using the GLAS Lidar-derived LAI amplitude reported in Tang and Dubayah (2017) for the Central Amazon region with an increase of 0.22 $\rm m^2/m^2$ from June to October, our ProSail model detected LAI forcing of only 1% on the predicted EVI (Table S1).

4. Discussion

Our findings confirm the dry season green-up effect over a large area in the Central Amazon as well as show strong associations between leaf phenology attributes measured at the canopy scale and satellite measurements. To our knowledge this is the most comprehensive study to date confirming the green-up phenomenon: we enact unprecedented experimental controls for sun-sensor geometry artifacts utilizing two independent orbital sensors (Landsat-8 and MODIS), thus combining high and coarse resolution remote sensing data, while also carefully accounting for topography and cloud contamination artifacts. Under all of these controls and data sources, results are consistent with green-up.

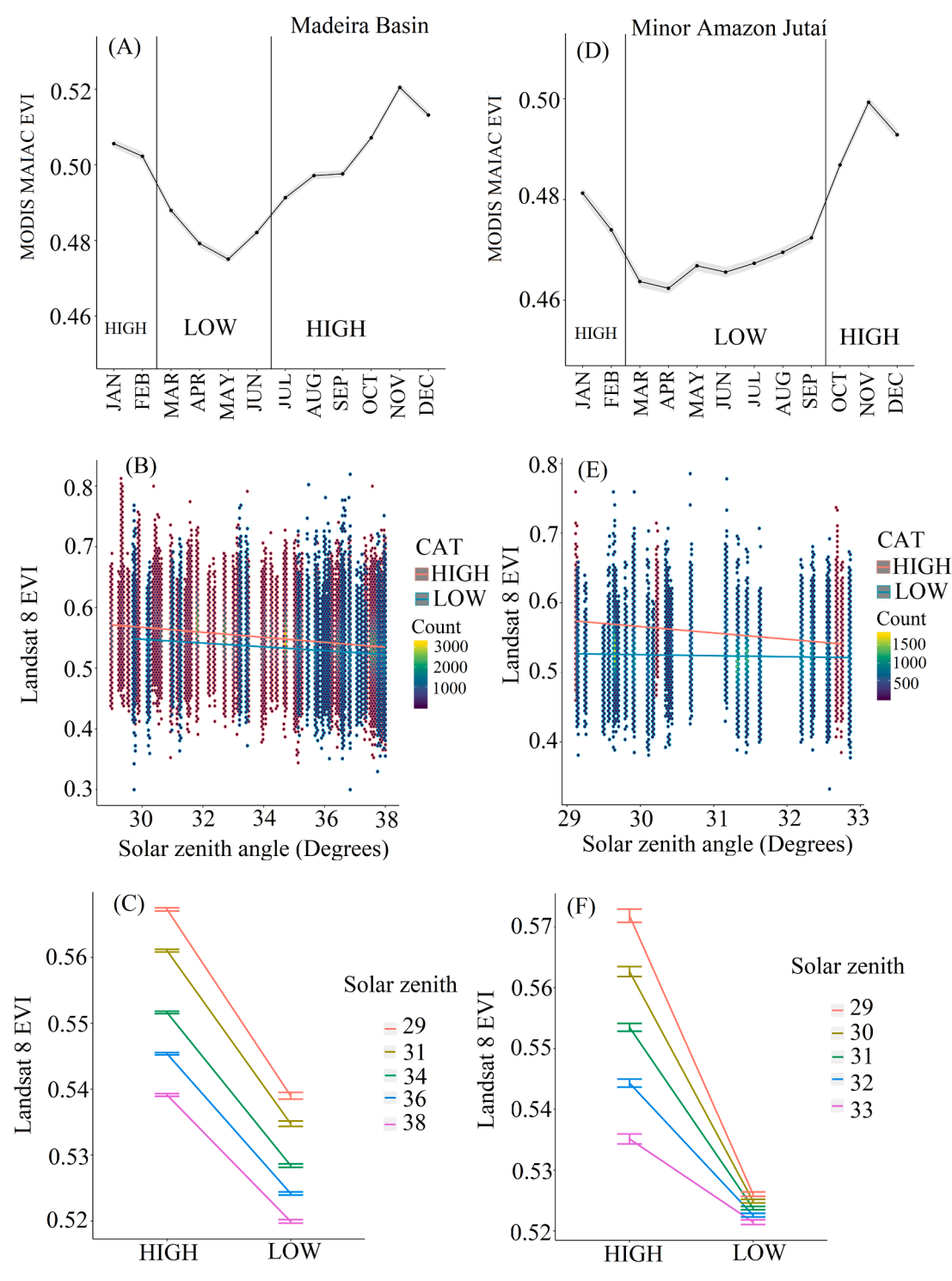


Fig. 4. (A) Modeled MODIS-MAIAC EVI seasonality controlling for HAND, Scene, and pixel ID as random effect (*Eq. 4*; we used 99% confidence levels) at the Madeira Basin comprising WRS scenes (Path_row): 229_66, 230_63, 230_64, 230_65, 230_66, 230_67, 231_64, 231_65, 231_66. MODIS-MAIAC data were collected within the same near Nadir view geometries used in the Landsat-8 analysis; Vertical lines identify periods in which EVI (HIGH/LOW) seasonal difference is more pronounced. Using these periods, Landsat-8 data is grouped to test if the seasonal predictions from MODIS-MAIAC are consistent with Landsat-8 when sun geometry is controlled. (B) Landsat-8 EVI at the near Nadir view within the scenes discussed in (A) comprising 99 images plotted against the Solar zenith angle. As mentioned before, Landsat-8 data were grouped into periods of the year with HIGH (JAN, FEB, JUL, AUG, SEP, OCT, NOV and DEC) and LOW EVI (MAR, APR, MAY, JUN) as predicted by MODIS-MAIAC EVI. Red dots represent periods of HIGH EVI and blue low EVI; (C) The partial effect of categorical variables (HIGH/LOW) and the solar zenith angle on Landsat-8 EVI (*Eq. (2*)) when the other predictors (HAND, fraction of free pixels, scene, and Pixel identity) are held constant. The error bars indicate confidence intervals with 99% of significance; (D) Same as (A) but now for the Minor Amazon Jutaí basin comprising Landsat-8 WRS scenes: 2_62, 2_63, 3_63, 3_64; (E) Same as (B) but for the Minor Amazon Jutaí basin comprising 35 Landsat-8 images; These scenes were grouped into periods of the year with HIGH (JAN, FEB, OCT, NOV and DEC) and LOW EVI (MAR, APR, MAY, JUN,JUL, AUG, SEP) (F) Same as (C) but for the Minor Amazon Jutaí basin. (For interpretation of the references to color in this figure legend, the reader is referred to the web version of this article.)

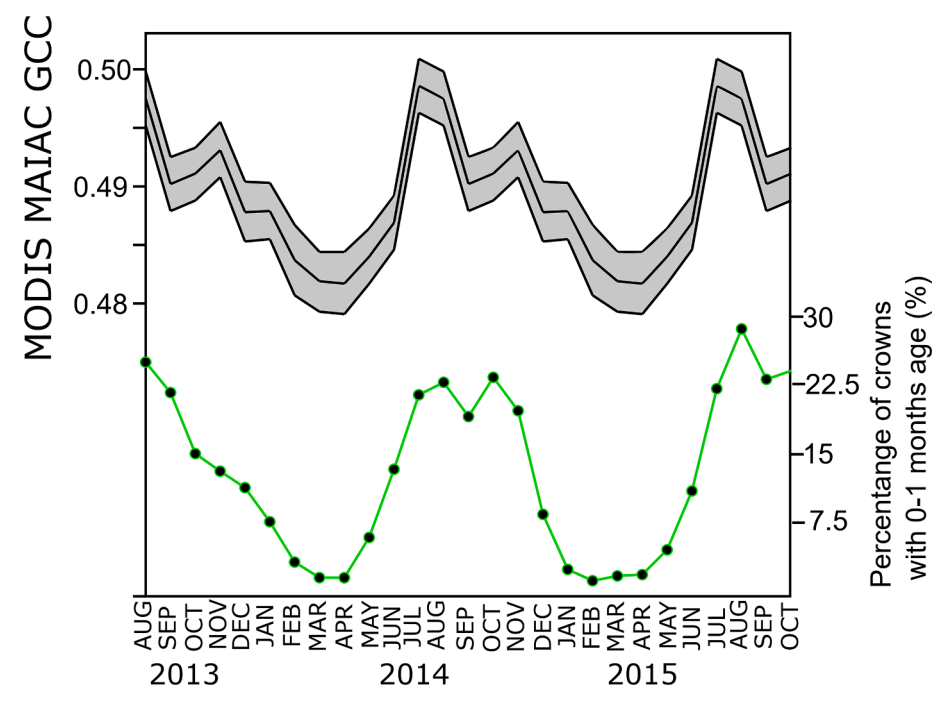


Fig. 5. Light green lines represent young leaves (0 to 1 month of age) abundance registered at the phenocam at the ATTO tower site from 2013 to 2015; The gray shaded area the is the seasonal MODIS-MAIAC GCC (95% CI) at the same site using a small 8X11km window centered at the ATTO site. (For interpretation of the references to color in this figure legend, the reader is referred to the web version of this article.)

Our findings provide a robust biophysical interpretation of VIs seasonality, which has previously been lacking (Maeda et al., 2016). Robust biophysical interpretation was achieved in primarily two ways: first, by validating BRDF-corrected MODIS-MAIAC seasonality signal using a 30 m resolution sensor while performing very robust controls of off-nadir view angles of Landsat; Second, by showing consistent links in observations from leaf demography derived from phenocams with MODIS-MAIAC. In conjunction with other recent and past studies, the present study contributes to a large body of evidence showing that Amazon dry-season green-up is real, with leaf phenology most likely the dominant driving force (Bi et al., 2015; Guan et al., 2015; Saleska et al., 2016; Lopes et al., 2016; Moura et al. 2017; Wu et al., 2018; Gonçalves et al., 2019; Gonçalves et al., 2020; Wang et al., 2020; Hashimoto et al., 2021).

4.1. GCC, EVI and NIR for MODIS-MAIAC and Landsat-8, when controlling sun-sensor geometry:

Using approach 1 – Comparing pixels with the same phase angle in different parts of the images – we found evidence that in the Central Amazon the average landscape greenness in the visible portion of the spectrum, as represented by GCC, is highest in mid dry season, lowest in mid wet season and intermediate at the wet to dry transition. The Landsat-8 seasonal ranking of GCC follows the same ranking observed for both seasonal and the closest date MODIS-MAIAC GCC. In the continuous MODIS data this seasonal ranking is part of a monomodal visible spectrum green-up, with a peak in the early to mid-dry season. We also found evidence that EVI seasonality is consistent in both Landsat-8 and MODIS-MAIAC showing the same ranking for approach 1 at scene 230_63, where EVI was lower in the late wet season, intermediate at the dry season, and higher in the early wet season illustrating the seasonal green-up.

Our approach 2 for addressing our first question — with near-nadir view and nearly identical solar zeniths for the two Landsat dates of a single scene (230_61) that includes the ATTO tower — also showed strong NIR and EVI seasonality, both increasing from May to December in the same year of 2015, as also seen in local MODIS-MAIAC data. The NIR

increase was large, about 13%. Fully eliminating sun-sensor geometry differences between the two Landsat seasonal acquisitions leaves little doubt about EVI and NIR seasonal green-up. These results do not support the conclusions of Morton et al. (2014) that EVI greenness is consistent throughout the year after artifacts are taken into account. This approach, instead, shows the consistency of the seasonality within the same year, while approach 1 uses images from different years that could be affected by interannual variations.

For both approach 1 and 2 the seasonal amplitudes for EVI and GCC from the two sensors were slightly different, with Landsat-8 consistently higher (Fig. 2A, 2B) than MODIS-MAIAC (Fig. 2C, 2D). This was expected for several reasons. First, the MODIS-MAIAC BRDF correction emulates a phase angle of 45° while our Landsat-8 scenes use pixels that have phase angles of about 36°. For example a larger phase angle increases sub-pixel shade, reducing NIR reflectance, which in turn reduces EVI. Second, the phase angle effects may not be completely linear such that the ratio of increase/decrease could be different when the same area under comparison has distinct phase angles in both products. Third, we used single date EVI values with Landsat, but 16 day mosaics for MODIS, which could cause smoothing and add noise to the data. Fourth, the coarse resolution of MODIS-MAIAC, 1 km × 1 km, could still include small clouds, topographic shadow, and floodplain forests of small streams phenologically out of phase with upland forest. With Landsat 30 m data, we were able to limit analysis to flat, well-drained soils free from topographic shadows, clouds and cloud shadow. Finally, minor discrepancies in bandwidth between Landsat-8 and MODIS may also play a role and need to be investigated further.

Our third approach for addressing our first question extends the results of the two previous approaches to a much larger area of the Amazon Basin, while also considering possible caveats previously mentioned. The seasonal green-up patterns for Landsat-8 and MODIS-MAIAC were consistent across all sub-basins. Five sub-basins (Madeira, Purus 2, Negro, Tapajos, and Trombetas) show similar changes in EVI values between HIGH and LOW local EVI time periods in terms of percentage change for both Landsat-8 and MODIS-MAIAC (Fig. S3, black dots). The other four sub-basins (Purus 1, Minor Uatuma, Jutai, and Xingu) also exhibited a directional seasonal change

- Camera total canopy LAI
- Mature leaves (2-7 months)

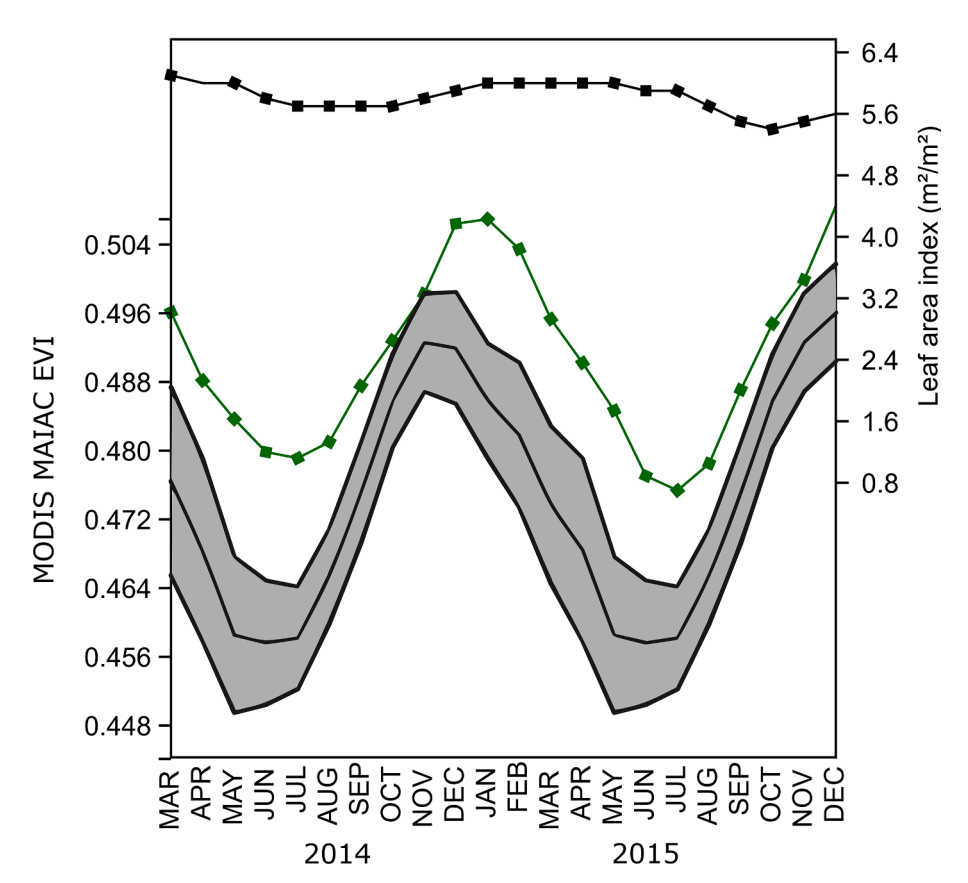


Fig. 6. Black solid line on the top represents the camera-based total canopy Leaf area index (LAI) and the green solid line is LAI for mature leaves (2 to 7 months of age) derived from the RGB camera mounted at the ATTO site. The gray shaded lines are the seasonal MODIS-MAIAC EVI (95% CI) repeated from March of 2014 to December 2015 also for the ATTO site. (For interpretation of the references to color in this figure legend, the reader is referred to the web version of this article.)

in EVI for both products, although percentage changes were less numerically consistent. Two reasons are suggested here, while the arguments advanced in the last paragraph for approaches 1 and 2 apply as well. First, the overlapping pixels available for the two sensors encompassed only a small variation in solar zenith angle. Therefore, the statistical model may not be capable of accounting for the full effect of solar zenith angle on EVI. Second, the Landsat-8 time series spans 2013 to 2021 while the MODIS-MAIAC data window has a larger temporal overlap (2001–2016) and excludes some drought periods.

Given that we are consistently comparing flat, well-drained oldgrowth upland forests within the same scene, the consideration of spatial structure did not affect our main results, as shown by generalized additive models for all three of our approaches. This supports our first assumption that sets of usable pixels available on each date represent the average scene signal on that date.

4.2. EVI and canopy leaf demography in the Central Amazon

EVI may be sensitive to changes in LAI, and canopy leaf area structure. While this is not easy to measure in the Amazon, the most advanced approaches to date that capture vertical shifts in leaf area over seasonality (Tang and Dubayah, 2017; Smith et al., 2019) show relatively little change in total leaf area. Our Prosail Modeling effort showed that this was too little to account for the 9% change detected with MODIS-MAIAC at the ATTO site. Furthermore, monthly values of upper canopy LAI (based on the monthly fraction of green crowns in tower camera view)

were a poor predictor of seasonal variability in MODIS-MAIAC EVI. Upper canopy LAI thus appears not to be the main driver of change in the spectral signal, at least in the Central Amazon. Instead, our results strongly suggest that upper canopy leaf age - especially the fraction of crowns having mature leaves 2-7 months old - drives seasonality of the EVI signal. Laboratory spectra of tropical forest leaves of known age also show higher NIR reflectance for mature leaves (Roberts er al., 1998; Chavana-Bryant et al., 2016; Moura et al., 2017; Wu et al., 2018). This study also confirms and extends observations by Lopes et al. (2016) and Wu et al. (2018), that leaf quality, not leaf amount, is the main control over the seasonal remote sensing signal. In regions with longer dry seasons, however, where the LAI has a larger range of seasonal variation, EVI could be effectively controlled more by canopy LAI than by leaf demography (Restrepo-Coupe et al., 2013; Song et al., 2021). EVI-based inversions that use canopy biophysical parameters such as the LAI (Hilker et al., 2017) should therefore be considered cautiously.

4.3. Biophysical control of GCC in the Central Amazon

GCC was also associated with the year-round upper canopy leaf demography derived from tower-mounted RGB cameras. Lopes et al. (2016) found that recently flushed crowns have high GCC relative to other crown phenostages. In the three drier months of June to August, close to 50% of all crowns flushed new leaves at their ATTO tower study site, while in the three months of December to February only about 8% of crowns flushed out new leaves. Our results also confirm and extend

those of Gonçalves et al., 2019 regarding GCC seasonality in Landsat-8 OLI

4.4. Implications for photosynthetic seasonality modeling in Amazon evergreen forests

Our results strongly indicate that the MODIS GCC signal at the ecosystem scale is sensitive to the abundance of crowns with recently flushed a cohort of new leaves while the MODIS EVI is sensitive to the abundance of mature leaves. Young leaves have lower intrinsic photosynthetic capacity (Vcmax), compared to mature leaves (Wu et al., 2016; Albert et al., 2018). Future efforts should leverage this information to model basin-wide seasonal primary productivity from coupled GCC and EVI MODIS data.

5. Conclusions

Across two Landsat-8 OLI scenes, we validate BRDF corrected MODIS-MAIAC EVI and GCC seasonality, obtained under fixed sunsensor geometry at different seasons. We extend the validation of MODIS-based EVI seasonality, including dry season EVI green-up, to eight large sub-basins of the Amazon, and show that it is consistent with EVI seasonality derived from Landsat-8. At two additional Central Amazon tower sites, we corroborate the radiative transfer model-based conclusions of Wu et al (2018), previously shown for only a single tower site: LAI is a poor or minor driver of the seasonal change in Central Amazon Forest EVI as detected by orbital sensors, while the change in leaf reflectance spectra with leaf age and change in the seasonal abundance of mature leaves, 2-7 months old as detected by phenocams are the main drivers of seasonal EVI. We also found a novel result that MODIS GCC seasonality is consistent with the seasonal abundance of the recently flushed (0-1 mo old) age class as detected by tower-mounted RGB cameras and seasonal leaf litter production.

Declaration of Competing Interest

The authors declare that they have no known competing financial interests or personal relationships that could have appeared to influence the work reported in this paper.

Acknowledgements

We thank the Max Planck Society and Brazil's National Institute for Amazon Research. The Amazon Tall Tower construction, instrumentation and maintenance are supported by the German Federal Ministry of Education and Research (BMBF contract 01LB1001A), the Brazilian Ministry of Science, Technology and Innovation (MCTI/FINEP contract 01.11.01248.00), the Amazonas State University (UEA), FAPEAM, LBA/ INPA and SDS/CEUC/RDS-Uatuma. The Amazonas State Foundation for Research Support (FAPEAM) financed the GoAmazon project "Understanding the Response of Photosynthetic Metabolism in Tropical Forests to Seasonal Climate Variations" (PI Marciel José Ferreira). We thank Yujie Wang and Alexei Lyapustin from NASA for providing freely available MODIS-MAIAC data. R.D. was supported by the São Paulo Research Foundation (FAPESP) grant 2019/21662-8. J.W. was supported by National Natural Science Foundation of China (# 31922090), and in part supported by the Innovation and Technology Fund (funding support to State Key Laboratory in Hong Kong of Agrobiotechnology) of the HKSAR, China.. SC Stark was supported by NSF DEB awards no. 1950080 and 1754357. NB Gonçalves was financed in part by the Coordenação de Aperfeiçoamento de Pessoal de Nível Superior - Brasil (CAPES) -Finance code 001 and by Michigan State University Mericle Memorial Fund.

Appendix A. Supplementary data

Supplementary data to this article can be found online at https://doi.org/10.1016/j.isprsjprs.2022.12.001.

References

- Albert, L., Wu, J., Prohaska, N., Camargo, P., Huxman, T., Tribuzy, E., et al., 2018. Age-dependent leaf physiology and consequences for crown-scale carbon uptake during the dry season in an Amazon evergreen forest. New Phytol. 219 (3), 870–884. https://doi.org/10.1111/nph.15056.
- Bi, J., Knyazikhin, Y., Choi, S., Park, T., Barichivich, J., Ciais, P., et al., 2015. Sunlight mediated seasonality in canopy structure and photosynthetic activity of Amazonian rainforests. Environ. Res. Lett. 10 (6), 064014 https://doi.org/10.1088/1748-9326/ 10/6/064014.
- Brando, P., Goetz, S., Baccini, A., Nepstad, D., Beck, P., Christman, M., 2010. Seasonal and interannual variability of climate and vegetation indices across the Amazon. Proc. Natl. Acad. Sci. 107 (33), 14685–14690. https://doi.org/10.1073/ pnas.0908741107.
- Candra, D., Phinn, S., & Scarth, P. (2016). Cloud and cloud shadow masking using multitemporal cloud masking algorithm in tropical environmental. ISPRS - International Archives Of The Photogrammetry, Remote Sensing And Spatial Information Sciences, XLI-B2, 95-100. Doi: https://doi.org/10.5194/isprsarchives-xli-b2-95-2016
- Conrad, O., Bechtel, B., Bock, M., Dietrich, H., Fischer, E., Gerlitz, L., et al., 2015. System for Automated Geoscientific Analyses (SAGA) v. 2.1.4. Geosci. Model Dev. 8 (7), 1991–2007. https://doi.org/10.5194/gmd-8-1991-2015.
- Chavana-Bryant, C., Malhi, Y., Wu, J., Asner, G., Anastasiou, A., Enquist, B., et al., 2016. Leaf aging of Amazonian canopy trees as revealed by spectral and physiochemical measurements. New Phytol. 214 (3), 1049–1063. https://doi.org/10.1111/nph.13853.
- Dalagnol, R., Galvão, L.S., Wagner, F.H., Moura, Y.M., Gonçalves, N., Wang, Y., Aragão, L.E.O.C., 2022. AnisoVeg: Anisotropy and Nadir-normalized MODIS MAIAC datasets for satellite vegetation studies in South America. Earth Syst. Sci. Data Discuss. 1–19.
- Donchyts, G., et al. (2016). Global 30m Height Above the Nearest Drainage Global 30m Height Above the Nearest Drainage New elevation dataset normalized according to the local height found along the drainage network. EGU European Geosciences Union,(April), 2–3. Doi: https://doi.org/10.13140/RG.2.1.3956.8880.
- Fasiolo, M., Nedellec, R., Goude, Y., Wood, S., 2019. Scalable Visualization Methods for Modern Generalized Additive Models. J. Comput. Graph. Stat. 29 (1), 78–86. https://doi.org/10.1080/10618600.2019.1629942.
- Galvão, L., dos Santos, J., Roberts, D., Breunig, F., Toomey, M., de Moura, Y., 2011. On intra-annual EVI variability in the dry season of tropical forest: A case study with MODIS and hyperspectral data. Remote Sens. Environ. 115 (9), 2350–2359. https:// doi.org/10.1016/j.rse.2011.04.035.
- Fox, J., 2003. Effect Displays in R for Generalised Linear Models. J. Stat. Softw. 8 (15), 1–27 http://www.jstatsoft.org/v08/i15/.
- Galvão, L., Breunig, F., Teles, T., Gaida, W., Balbinot, R., 2016. Investigation of terrain illumination effects on vegetation indices and VI-derived phenological metrics in subtropical deciduous forests. Gisci. Remote Sens. 53 (3), 360–381. https://doi.org/ 10.1080/15481603.2015.1134140.
- Gonçalves, N., Lopes, A., Dalagnol, R., Wu, J., Pinho, D., Nelson, B., 2020. Both near-surface and satellite remote sensing confirm drought legacy effect on tropical forest leaf phenology after 2015/2016 ENSO drought. Remote Sens. Environ. 237, 111489 https://doi.org/10.1016/j.rse.2019.111489.
- Guan, K., Pan, M., Li, H., Wolf, A., Wu, J., Medvigy, D., et al., 2015. Photosynthetic seasonality of global tropical forests constrained by hydroclimate. Nat. Geosci. 8 (4), 284–289. https://doi.org/10.1038/ngeo2382.
- Hashimoto, H., Wang, W., Dungan, J., Li, S., Michaelis, A., Takenaka, H., et al., 2021. New generation geostationary satellite observations support seasonality in greenness of the Amazon evergreen forests. Nature. Communications 12 (1). https://doi.org/ 10.1038/s41467-021-20994-y.
- Hijmans, R.J. (2016). raster: Geographic Data Analysis and Modeling. R package version 2.5-8. URL: https://CRAN.R-project.org/package=raster.
- Hess, L., Melack, J., Affonso, A., Barbosa, C., Gastil-Buhl, M., Novo, E., 2015. Wetlands of the Lowland Amazon Basin: Extent, Vegetative Cover, and Dual-season Inundated Area as Mapped with JERS-1 Synthetic Aperture Radar. Wetlands 35 (4), 745–756. https://doi.org/10.1007/s13157-015-0666-y.
- Hilker, T., Galvão, L., Aragão, L., de Moura, Y., do Amaral, C., & Lyapustin, A. et al. (2017). Vegetation chlorophyll estimates in the Amazon from multi-angle MODIS observations and canopy reflectance model. International Journal Of Applied Earth Observation And Geoinformation, 58, 278-287.
- Huete, A., Didan, K., Shimabukuro, Y., Ratana, P., Saleska, S., Hutyra, L., et al., 2006. Amazon rainforests green-up with sunlight in dry season. Geophys. Res. Lett. 33 (6) https://doi.org/10.1029/2005gl025583.
- Jacquemoud, S., Verhoef, W., Baret, F., Bacour, C., Zarco-Tejada, P., Asner, G., et al., 2009. PROSPECT+SAIL models: A review of use for vegetation characterization. Remote Sens. Environ. 113, S56–S66. https://doi.org/10.1016/j.rse.2008.01.026.
- Jiang, Z., Huete, A., Didan, K., Miura, T., 2008. Development of a two-band enhanced vegetation index without a blue band. Remote Sens. Environ. 112 (10), 3833–3845. https://doi.org/10.1016/j.rse.2008.06.006.

- Lehnert, L., Meyer, H., Obermeier, W., Silva, B., Regeling, B., Bendix, J., 2019. Hyperspectral Data Analysis in R: The hsdar Package. J. Stat. Softw. 89 (12) https://doi.org/10.18637/jss.v089.i12.
- Lopes, A., Nelson, B., Wu, J., Graça, P., Tavares, J., Prohaska, N., et al., 2016. Leaf flush drives dry season green-up of the Central Amazon. Remote Sens. Environ. 182, 90–98. https://doi.org/10.1016/j.rse.2016.05.009.
- Lyapustin, A., Wang, Y., Laszlo, I., Hilker, T., G.Hall, F., & Sellers, P. et al. (2012). Multiangle implementation of atmospheric correction for MODIS (MAIAC): 3. Atmospheric correction. Remote Sensing Of Environment, 127, 385-393. Doi: https://doi.org/10.1016/j.rse.2012.09.002.
- Maeda, E., Galvão, L., 2015. Sun-sensor geometry effects on vegetation index anomalies in the Amazon rainforest. Giscience & Remote Sensing 52 (3), 332–343. https://doi. org/10.1080/15481603.2015.1038428.
- Maeda, E., Moura, Y., Wagner, F., Hilker, T., Lyapustin, A., Wang, Y., Chave, J., Möttus, M., Aragão, L., Shimabukuro, Y., 2016. Consistency of vegetation index seasonality across the Amazon rainforest. International Journal of Applied Earth Observation and Geoinformation 52, 42–53. https://doi.org/10.1016/j. jag.2016.05.005.
- Malhi, Y., Aragao, L., Galbraith, D., Huntingford, C., Fisher, R., Zelazowski, P., et al., 2009. Exploring the likelihood and mechanism of a climate-change-induced dieback of the Amazon rainforest. Proc. Natl. Acad. Sci. 106 (49), 20610–20615. https://doi. org/10.1073/pnas.0804619106.
- Morton, D., Nagol, J., Carabajal, C., Rosette, J., Palace, M., Cook, B., et al., 2014. Amazon forests maintain consistent canopy structure and greenness during the dry season. Nature 506 (7487), 221–224. https://doi.org/10.1038/nature13006.
- Moura, Y., Galvão, L., dos Santos, J., Roberts, D., Breunig, F., 2012. Use of MISR/Terra data to study intra- and inter-annual EVI variations in the dry season of tropical forest. Remote Sens. Environ. 127, 260–270. https://doi.org/10.1016/j. rse.2012.09.013.
- Moura, Y., Hilker, T., Lyapustin, A., Galvão, L., dos Santos, J., Anderson, L., et al., 2015. Seasonality and drought effects of Amazonian forests observed from multi-angle satellite data. Remote Sens. Environ. 171, 278–290. https://doi.org/10.1016/j. rse.2015.10.015.
- Moura, Y., Galvão, L., Hilker, T., Wu, J., Saleska, S., do Amaral, C., et al., 2017. Spectral analysis of amazon canopy phenology during the dry season using a tower hyperspectral camera and modis observations. ISPRS J. Photogram. Remote Sens. 131, 52–64. https://doi.org/10.1016/j.isprsjprs.2017.07.006.
- Ourique, L., Silva, R., Souza, C., Noguchi, H., Santos, J., Higuchi, N., 2016. Relação da produção de serapilheira com incremento em diâmetro de uma floresta madura na Amazônia Central. Scientia Forestalis 44 (112).
- Ponzoni, F. J., Shimabukuro, Y. E., & Kuplich, T. M. (2007). Sensoriamento remoto no estudo da vegetação (p. 127). São José dos Campos: Parêntese.
- R Core Team (2017). R: A language and environment for statistical computing. R Foundation for Statistical Computing, Vienna, Austria. URL: https://www.R-project.org/.
- Rennó, C., Nobre, A., Cuartas, L., Soares, J., Hodnett, M., Tomasella, J., Waterloo, M., 2008. HAND, a new terrain descriptor using SRTM-DEM: Mapping terra-firme rainforest environments in Amazonia. Remote Sens. Environ. 112 (9), 3469–3481. https://doi.org/10.1016/j.rse.2008.03.018.
- Restrepo-Coupe, N., da Rocha, H., Hutyra, L., da Araujo, A., Borma, L., Christoffersen, B., et al., 2013. What drives the seasonality of photosynthesis across the Amazon basin? A cross-site analysis of eddy flux tower measurements from the Brasil flux network. Agric. For. Meteorol. 182–183, 128–144. https://doi.org/10.1016/j.agrformet.2013.04.031.
- Roberts, D., Nelson, B., Adams, J., Palmer, F., 1998. Spectral changes with leaf aging in Amazon caatinga. Trees 12 (6), 315. https://doi.org/10.1007/s004680050157.
- Roy, D., Zhang, H., Ju, J., Gomez-Dans, J., Lewis, P., Schaaf, C., et al., 2016. A general method to normalize Landsat reflectance data to nadir BRDF adjusted reflectance. Remote Sens. Environ. 176, 255–271. https://doi.org/10.1016/j.rse.2016.01.023.

- Saleska, S., Didan, K., Huete, A., da Rocha, H., 2007. Amazon Forests Green-Up During 2005 Drought. Science 318 (5850). https://doi.org/10.1126/science.1146663.
- Saleska, S., Wu, J., Guan, K., Araujo, A., Huete, A., Nobre, A., Restrepo-Coupe, N., 2016. Dry-season greening of Amazon forests. Nature 531 (7594), E4–E5. https://doi.org/10.1038/nature16457.
- Smith, M., Stark, S., Taylor, T., Ferreira, M., de Oliveira, E., Saleska, S., et al., 2019. Seasonal and drought-related changes in leaf area profiles depend on height and light environment in an Amazon forest. New Phytol. 222 (3), 1284–1297.
- Solano, R., Didan, K., Jacobson, A., Huete, A., 2010. MODIS vegetation index user's guide (MOD13 series). The University of Arizona, Tucson, p. 38 pp.
- Song, G., Wu, S., Lee, C., Serbin, S., Wolfe, B., Ng, M., et al., 2021. Monitoring leaf phenology in moist tropical forests by applying a superpixel-based deep learning method to time-series images of tree canopies. ISPRS J. Photogram. Remote Sens. 183, 19–33. https://doi.org/10.1016/j.isprsjprs.2021.10.023.
- Sonnentag, O., Hufkens, K., Teshera-Sterne, C., Young, A., Friedl, M., Braswell, B., et al., 2012. Digital repeat photography for phenological research in forest ecosystems. Agric. For. Meteorol. 152, 159–177. https://doi.org/10.1016/j. agrformet.2011.09.009.
- Tang, H., Dubayah, R., 2017. Light-driven growth in Amazon evergreen forests explained by seasonal variations of vertical canopy structure. Proc. Natl. Acad. Sci. 114 (10), 2640–2644. https://doi.org/10.1073/pnas.1616943114.
- Valeriano, D.M., Mello, E.M.K., Moreira, J.C., Shimabukuro, Y.E., Duarte, V., Souza, I.M., Souza, R.C.M., et al., 2004. Monitoring tropical forest from space: the PRODES digital project. Int. Arch. Photogramm. Remote Sens. Spatial Informat. Sci. 35, 272–274.
- Venticinque, E., Forsberg, B., Barthem, R., Petry, P., Hess, L., Mercado, A., et al., 2016. An explicit GIS-based river basin framework for aquatic ecosystem conservation in the Amazon. Earth Syst. Sci. Data 8 (2), 651–661. https://doi.org/10.5194/essd-8-651-2016
- Wu, J., Kobayashi, H., Stark, S., Meng, R., Guan, K., Tran, N., et al., 2018. Biological processes dominate seasonality of remotely sensed canopy greenness in an Amazon evergreen forest. New Phytol. 217 (4), 1507–1520. https://doi.org/10.1111/ nph.14939.
- Yang, J., Tian, H., Pan, S., Chen, G., Zhang, B., Dangal, S., 2018. Amazon drought and forest response: Largely reduced forest photosynthesis but slightly increased canopy greenness during the extreme drought of 2015/2016. Glob. Chang. Biol. 24 (5), 1919–1934. https://doi.org/10.1111/gcb.14056.
- Wang, J., Yang, D., Detto, M., Nelson, B., Chen, M., Guan, K., et al., 2020. Multi-scale integration of satellite remote sensing improves characterization of dry-season green-up in an Amazon tropical evergreen forest. Remote Sens. Environ. 246, 111865. https://doi.org/10.1016/j.rse.2020.111865.
- Gonçalves, N., Lopes, A., Silva, R., Wu, J., Nelson, B., (2019). Confirming dry-season green-up in central amazon forests with landsat 8 and the role of leaf demography in modis-maiac seasonal spectral patterns. *Brazilian Symposium of remote sensing*. (Retrieved from:) https://www.researchgate.net/publication/335313480. CONFIRMING_DRY-SEASON_GREEN-UP_IN_CENTRAL_AMAZON_FORESTS_WITH_LANDSAT_8_AND_THE_ROLE_OF_LEAF_DEMOGRAPHY_IN_MODIS-MAIAC_SEASONAL_SPECTRAL_PATTERNS.
- Wood, S.N. (2017) Generalized Additive Models: An Introduction with R (2nd edition). Chapman and Hall/CRC.
- Wu, J., Albert, L., Lopes, A., Restrepo-Coupe, N., Hayek, M., Wiedemann, K., et al., 2016a. Leaf development and demography explain photosynthetic seasonality in Amazon evergreen forests. Science 351 (6276), 972–976. https://doi.org/10.1126/ science.aad5068.
- Wu, J., Chavana-Bryant, C., Prohaska, N., Serbin, S., Guan, K., Albert, L., et al., 2016b. Convergence in relationships between leaf traits, spectra and age across diverse canopy environments and two contrasting tropical forests. New Phytol. 214 (3), 1033–1048. https://doi.org/10.1111/nph.14051.